Performance of an open-path near infrared measurement system for measurements of CO_2 and CH_4 during extended field trials.

Nicholas M. Deutscher[1], Travis A. Naylor[1], Christopher G.R. Caldow[1,2], Hamish L. McDougall[1], Alex G. Carter[1,†], and David W.T. Griffith[1]

[1]Centre for Atmospheric Chemistry, School of Earth, Atmospheric and Life Sciences, Faculty of Science, Medicine and Health, University of Wollongong, Wollongong, NSW, 2522, Australia
[2]Now at Laboratoire des Sciences du Climat et de l'Environnement, LSCE/IPSL, CEA-CNRS-UVSQ, Universite Paris-Saclay, Gif-sur-Yvette, F-91191, France
[†]deceased, 8 September 2020

Correspondence: Nicholas M. Deutscher (ndeutsch@uow.edu.au)

Abstract. Open-path measurements of atmospheric composition provide spatial averages of trace gases that are less sensitive to small-scale variations and the effects of meteorology. In this study we introduce improvements to Open-Path Near Infrared (OP-NIR) Fourier Transform Spectrometer measurements of CO_2 and CH_4. In an extended field trial, the OP-NIR achieved measurement repeatability six times better for CO_2 (0.28 ppm) and ten times better for CH_4 (2.1 ppb) over a 1.55 km one-way path than its predecessor. The measurement repeatability was independent of pathlength up to 1.55 km, the longest distance tested. Comparisons to co-located in situ measurements under well-mixed conditions characterise biases of 1.41% for CO_2 and 1.61% for CH_4 relative to in situ measurements calibrated to World Meteorological Organisation - Global Atmosphere Watch (WMO-GAW) scales. The OP-NIR measurements can detect signals due to local photosynthesis and respiration, and local point sources of CH_4. The OP-NIR is well-suited for deployment in urban or rural settings to quantify atmospheric composition on kilometre scales.

Copyright statement. TEXT

1 Introduction

Anthropogenic greenhouse gases, primarily carbon dioxide (CO_2) and methane (CH_4), are the main drivers of systematic changes in the Earth's climate, especially a net warming of the atmosphere and oceans. Characterising sources and sinks of greenhouse gases to and from the atmosphere is critical to understanding past, present, and future change.

Open-path measurements of atmospheric composition can provide complementary information to that available from in situ point measurements. By integrating over kilometre-length scales, open-path measurements provide quantifications that are less sensitive to small-scale variability and more representative of model spatial scales. In applications around detecting remote

point sources, an integrated path also improves the likelihood of sampling through an emission plume. These advantages may
20   come at the cost of precision and accuracy compared to in situ point measurements.

Technologies available for open-path measurements include differential optical absorption spectroscopy (DOAS), differential absorption lidar (DIAL), integrated path differential absorption (IPDA) lidar, Chirped Laser Dispersion Spectroscopy (CLaDS) tunable diode laser absorption spectroscopy (TDLAS), frequency comb spectroscopy, and Open-Path FTIR (OP-FTIR).

25   Single wavelength open-path instruments include DIAL, IPDA, CLaDS and TDLAS. Tunable diode lasers are a relatively inexpensive technology capable of measurements of many atmospheric constituents, depending on the internal laser used. These have been applied to the detection of CO_2 and CH_4 in the past, but measured amounts vary considerably from instrument to instrument, and they are susceptible to drifts and inaccuracies (Feitz et al., 2018). CLaDS techniques, which rely on the phase of detected light, have been used for open-path measurements of methane (Nikodem et al., 2015; Plant et al., 2015). DIAL is
30   a LIDAR-based technique, that uses the differential backscatter signal between two wavelengths, one of strong absorption and the other of weak, to quantify concentrations of atmospheric absorbers. IPDA is a variant of DIAL, using topographical targets to allow integrated-path measurements. DIAL (Queisser et al., 2016) and IPDA (Wagner and Plusquellic, 2016) can be applied to integrated-path measurements of CO_2 and CH_4. In general, laser-based techniques can have low power requirements, but are only tuned around a single wavelength, and therefore can typically only detect a single gas. In addition this leaves them
35   susceptible to potential interferences. GreenLITE[TM] (Dobler et al., 2013; Lian et al., 2019) gets around some of the interference aspect by measuring at two wavelengths.

DOAS is typically applied in the ultraviolet and visible regions of the spectrum, making it unsuitable for measuring greenhouse gases. Recent advances have seen the expansion of DOAS-type measurements into the near infrared (NIR), delivering repeatability in CO_2 measurements of 2-4 ppm over km-scale pathlengths, and CH_4 repeatability on the order of 200 ppb (Saito
40   et al., 2015).

Frequency comb spectroscopy enables measurements across a range a spectral wavelengths. For example, Alden et al. (2019) employ a dual frequency comb spectrometer to measure methane, operating over a 270 cm^{-1} spectral window centred at 7000 cm^{-1} at high spectral resolution (0.0067 cm^{-1}). This combination of a wider window and high spectral resolution allows for the simultaneous retrieval of interfering species, especially atmospheric water vapour, improving the inherent stability and accuracy
45   of the measurement. The instruments can operate in different wavelength regions; Rieker et al. (2014) describe an earlier system operating around 6000 cm^{-1} at 0.0033 cm^{-1} resolution, which measures CO_2, CH_4, H_2O, HDO, and $^{13}CO_2$ over 2km pathlengths, with 5 min precision of better than 1 ppm for CO_2 and 3 ppb for CH_4 with agreement between instruments of better than 1 ppm CO_2 and 7 ppb for CH_4 (Waxman et al., 2017).

While not operating at the spectral resolutions achieved by laser-based spectroscopy, open-path FTIR spectrometers can
50   operate over even wider spectral regions, allowing quantification of many gases that absorb infrared radiation in the atmosphere. Open-path mid-infrared (OP-MIR) measurements (200 - 4000 cm^{-1}) are limited to relatively short pathlengths because of the low brightness of the internal MIR light source. Open-path MIR measurements have been used to quantify CO_2 and CH_4 on paths up to 400m (e.g. (Desservettaz et al., 2019; Phillips et al., 2019)) in an urban environment. More typically they have

been applied on 100m scales, for quantification of area sources coupled with a tracer gas, micrometerological techniques or a backward lagrangian stochastic model (WINDTRAX) (Bai et al., 2018; Flesch et al., 2016; Jones et al., 2011; Laubach et al., 2013; Loh et al., 2009; Naylor et al., 2016; Phillips et al., 2016). OP-MIR has also been used to detect and quantify a point CO_2 and CH_4 source during a controlled release experiment (Cartwright et al., 2019; Feitz et al., 2018). At these pathlengths, repeatability of 1 ppm CO_2 and 5 ppb for CH_4 can be achieved. Tomographic techniques for quantifying fluxes, such as described by Humphries et al. (2012), could be applied to open-path measurements.

Griffith et al. (2018) detailed a pilot study extending OP-FTIR to measurements in the near infrared (NIR) spectral region (4000 - 13,500 cm^{-1}), where higher source brightness results in better collimation of the beam, and theoretically longer paths. In addition, there are fewer interfering species, though the absorptions of CO_2 and CH_4 are weaker relative to MIR as they are overtone and combination bands. The instrument was deployed over a 1.55km one-way path, and demonstrated repeatability of 1.7 ppm for CO_2 and 21 ppb for CH_4 for 5 minute averages. This manuscript details further developments and field trials based on the instrument introduced in that study, and demonstrates significant improvements in precision and accuracy.

Section 2 describes the instrument, data processing and corrections applied to the data. The field deployment and testing of the instrument is described in Section 3, while the results are presented and discussed in Section 4. The conclusions are then presented in Section 5.

2 Open-path Near InfraRed Spectrometer

The instrument described here is based on the instrument described by Griffith et al. (2018), which was deployed in Heidelberg, Germany. We describe the instrument, retroreflector array and data processing, and highlight the modifications relative to Griffith et al. (2018).

Figure 1 shows a schematic of the instrument setup. The central component of the open-path NIR (OP-NIR) system is a low spectral resolution FTIR spectrometer, the Bruker IRcube (Bruker Optik, Ettlingen, Germany). The spectrometer has an internal 25W tungsten globe restricted to 11W as NIR radiation source, quartz beamsplitter and TE-cooled Indium Gallium Arsenide (InGaAs) detector optimised for the NIR spectral region, covering the spectral range from 3800 to 10,000 cm^{-1}. This covers the same spectral range as that used in the Total Carbon Column Observing Network (TCCON) (Wunch et al., 2011), which measures total column CO_2, CH_4 and other gases using the sun as a light source. Unlike TCCON, the IRcube used in this study has a low spectral resolution of 0.5 cm^{-1} (maximum optical path difference of 1.8 cm). The spectrometer is relatively compact (310 x 290 x 220 mm, 14 kg).

For this work, the relatively small spectrometer allows it to be mounted on an Automated Instrument Mount (AIM, Omegalec, Unanderra, NSW, Australia), previously also used for open-path MIR measurements. AIM allows programmable, adjustable pointing of the instrument, driven by stepper motors on each of a elevation and azimuth axis. AIM and the instrument are supported on a heavy-duty tripod (MOOG-QuickSet, Northbrook, IL, USA). The spectrometer is rigidly coupled to a beam-expanding telescope. In contrast to the setup used by Griffith et al. (2018), here we use a 50:50 zinc selenide (ZnSe) beamsplitter instead of an optic fibre to couple the interferometer and detector to the telescope, and a Schmidt-Cassegrain (Meade Instru-

ments Corporation, Irvine, CA, USA), instead of a Newtonian, telescope. In addition, the light is modulated prior to exiting the spectrometer, minimising the effects of stray light from the environment on the measurements. The telescope has the Schmidt corrector plate removed and uses a custom convex 30 mm diameter secondary mirror with 50 mm focal length mounted on a micrometer stage for fine focus adjustment to convert the telescope to a beam expander. Direct back reflection off centre of the secondary mirror to the beamsplitter, which would result in a shorter measurement path, is minimised by masking the centre of the secondary mirror using non-reflective material. This setup more closely resembles that used with existing OP-MIR systems (Flesch et al., 2016; Naylor et al., 2016; Phillips et al., 2016), and in initial lab and field trials provided an order of magnitude more throughput than the optic fibre coupling described by Griffith et al. (2018).

The retroreflector initially used was a hollow gold-coated corner cube array (30 x 63mm, PLX Inc, Deer Park, NY, USA) previously deployed with the OP-MIR systems. This was later replaced by an array of 49 x 50mm solid BK-7 glass retroreflectors (JEOC, Zhejiang, China) with a total dimension of 600 mm by 625 mm (height x width). The solid glass corner cubes are less prone to condensation and dust accumulation, easily cleaned, and require less maintenance in the field, as well as being considerably less expensive to purchase. The beam transmitted over the open path is returned to the telescope via the retroreflector array. The returning beam is reflected off the beamsplitter, and focussed onto the InGaAs detector in the spectrometer.

Auxiliary information is logged at the spectrometer end of the path. A temperature sensor (LM335 diode) is housed in a solar shield to protect from direct solar radiation, while a pressure sensor (Vaisala PTB110, Helsinki, Finland) is housed in a vented box. These are logged on the same time interval as spectral collection.

The instrument is powered by 240V mains power. For field deployment, it was housed in a portable aluminium garden shed.

2.1 Data processing

From the collected NIR spectra, path-averaged trace gas mole fractions are retrieved by fitting a calculated spectrum to the measured spectrum. The calculated spectrum is generated using a forward model, Multiple Atmospheric Layer Transmission (MALT, Griffith (1996)). The forward model uses absorption line parameters based on HITRAN 2016 (Gordon et al., 2017) (updated from HITRAN 2008 (Rothman et al., 2009) used in Griffith et al. (2018)), measured temperature, pressure and pathlength, and an initial estimate of trace gas amounts, together with an instrument model accounting for resolution, apodisation, lineshape, spectral shift and continuum shape. The calculated spectrum is iteratively adjusted using the Levenberg-Marquardt algorithm to achieve the best fit to the measured spectrum. This yields a path-integrated number of molecules (column density, molecules cm^{-2}), which is converted to a path-averaged mole fraction using the air density calculated from pressure and temperature. Spectra are fitted in a number of different windows. Those used for this work are summarised in Table 1 and are illustrated in Griffith et al. (2018).

Spectra are fitted in real time immediately after collection to provide an initial estimate of trace gas mole fractions; however, we subsequently re-fit the spectra to account for two corrections: 1) the residual back-reflection from the secondary mirror; and 2) differences between the temperature measured at one end of the path and the effective or true path-averaged temperature. The retrievals are corrected to dry-air mole fractions using the H_2O column retrieved from the spectra.

2.1.1 Short-path correction

A small fraction of the outgoing beam is reflected directly back from the centre of the convex secondary mirror to the beam-splitter and detector. Outgoing radiation can also be reflected by the external beamsplitter and returned to the beamsplitter and detector after diffuse reflection from the inside of the instrument cover. Both of these effects result in radiation that does not traverse the full atmospheric path. These effects are minimised by blocking the centre of the secondary mirror and shielding the instrument cover with a non-reflective, matt black surface. Despite these measures, the short-path signal is not completely eliminated, but remains relatively constant and is independent of the long-path intensity. It therefore represents a variable relative contribution to the total intensity.

For a more accurate analysis of the long-path spectrum, a correction for this effect is derived and applied. An off-target spectrum is recorded and stored by pointing the telescope away from the retroreflector to ensure there is no long-path contribution. A least-squares fit of the stored off-target spectrum is performed for each long-path measurement in the 5000 - 5500 cm^{-1} region, which is otherwise blacked out by H_2O absorption in the full path. The least-squares fit provides a scaling factor to apply to the stored off-target spectrum, which is then subtracted from the measured spectrum across the full wavelength range. The spectral analysis is then repeated on the resulting long-path only spectrum. Example long-path and short-path spectra are shown in Figure 2.

2.1.2 Path-averaged temperature

Temperature is required in the spectral analysis to generate the forward model spectrum from HITRAN line parameters, and to calculate air density when deriving mole fractions. Air density is directly inversely proportional to temperature, therefore a 1% error in absolute temperature will result in an inversely proportional error in mole fraction. The measured temperature at one end of the path is not necessarily representative of the effective mean temperature along the long-path due to variation of the temperature within the path and the possibility that the measured temperature could be influenced by solar radiation and thermal mass of surrounds. In general, the measured temperature is also likely to be made closer to the ground than the average measurement height (beam path) along the open path.

To determine the effective path-averaged temperature, an initial fit to the CO_2 window (Table 1) is performed including the temperature in the least-squares fit. The retrieved temperature is then applied as a fixed value in reanalysis of all windows. The retrieved temperatures show the greatest difference from the measurements during daytime, when solar heating of the sensor results in a positive bias in the apparent measured values and can be as much as 5-10 °C. Waxman et al. (2017) found that a similar process was necessary with frequency comb spectroscopy open-path measurements.

The net effect of the refitting process to account for both the short-path correction and path-averaged temperature yields the differences illustrated in Figure 3. The refitted temperatures are generally lower. This, together with removing the shortpath absorption, results in an increase in retrieved mole fractions after refitting.

5

3 Field deployment

After initial testing over short pathlengths within the lab and on the University of Wollongong campus, the instrument was deployed on an extended field campaign to a New South Wales Department of Primary Industries (NSW-DPI) agricultural research site, Elizabeth Macarthur Agricultural Institute (EMAI) at Menangle, NSW. The site is located just outside the current
155 Sydney urban area, 52 km to the south-west of the city. The location is depicted in the map in Figure 4.

The instrument was located on site for about four months (123 days), from August 4, 2018 to December 12, 2018. Throughout the deployment period, several changes to the setup took place, as summarised in Table 2. Firstly, the pathlength was varied by moving the retroreflector array from 0.6 km to 1.11 km to 1.55 km distant from the FTIR, resulting in total pathlengths of 1.20, 2.22 and 3.10 km. The terrain limited the one-way path to a maximum of 1500 m. At 600 m, the retroreflector array was
160 changed from the hollow gold-coated array to the array of BK7 glass corner cubes. Finally, the telescope was changed from a 10-inch to 12-inch version.

Accounting for two periods where the instrument was removed for 1) a re-alignment; and 2) the change in telescope size, the OP-NIR measured successfully during the remote deployment for 92% of the possible time. Data losses occurred due to power failures and on site instrument maintenance. After filtering to remove spectra with small signal due mostly to rain, fog
165 and condensation on the retroreflectors (less than 5% of the maximum) and poor fits (RMS residual greater than 0.007), a further 9% of measurements were removed, mostly due to moisture, meaning the system was able to provide measurements of path-averaged mole fractions 83% of the time.

3.1 Cavity RingDown Spectrometer (CRDS) in situ measurements

During the campaign, a Picarro G2301 Cavity RingDown Spectrometer (CRDS) (Crosson, 2008), measuring CO_2, CH_4 and
170 H_2O was deployed. The CRDS measured continuously and was co-located with the OP-NIR spectrometer from November 30 to December 12, 2018. The CRDS sampled from an inlet mounted above the roof of the instrument shed at approximately 2.5m above ground level. It was calibrated against a suite of WMO-traceable gas standards before and after the deployment and showed no drift in calibration during the period.

3.2 Meteorological data

175 Weather data are collected on site by NSW-DPI 1.2 km to the south-south-east of the OP-NIR instrument shelter. These are collected with 10 min resolution using a Measurement Engineering Australia all-in-one weather station, supplying wind speed and direction, temperature, humidity, solar radiation, and precipitation.

4 Results

The time series of CO_2, CH_4, O_2. H_2O, CO and N_2O from the EMAI deployment are shown in Figure 5. While the CO (120
180 $\pm$ 80 ppb (mean $\pm$ standard deviation)) and N_2O (330 $\pm$ 60 ppb) retrievals are centred on realistic values, the scatter about

these is large due to the transmission cutoff of the BK7 glass corner cubes at lower frequencies where these species absorb. This could be improved by using corner cubes of different glass or quartz, but the focus of the remainder of this work will be on CO_2 and CH_4.

4.1 Measurement performance

185 We assess the performance of the system using a variety of metrics. Firstly, we calculate the signal-to-noise ratio (SNR) within the spectra by ratioing consecutive spectra and calculating the root-mean-square (RMS) noise of the result in the 6300 - 6500 cm^{-1} spectral region, free from atmospheric absorption.

Secondly, we assess the repeatability of the path-averaged mole fraction measurements by choosing periods when atmospheric variability is small, specifically at windspeeds greater than 2 ms^{-1}. This does not eliminate all sources of real atmo-

190 spheric variability, therefore a low frequency running mean (40 points/2 hours) was also subtracted from the time series in order to assess the variability in the trace gas measurements. Allan deviations (Allan, 1966; Werle et al., 1993) are also calculated, and for single measurements agree with the standard deviations of the noise time series.

The results are summarised in Table 3 for varying pathlengths and instrument setups with the results from the original Heidelberg deployment (Griffith et al., 2018) for comparison. A change of retroreflector array at 600m pathlength yields

195 SNR improvement of about a factor of three, and a small improvement in trace gas retrieval repeatability for CO_2 (18%) and CH_4 (44%), as shown in the difference in performance between measurement periods 1 and 2. The retroreflector arrays are nearly identical in size, therefore this is attributed to the newer, cleaner optics. Measurements of CO and N_2O are, however, compromised by the change in reflector due to lower transmission at these wavelengths through the glass corner cubes.

For a (constant) detector-noise limited spectrum measurement, increasing pathlength from 600m to 1110m to 1500m would

200 decrease spectrum signal and SNR as the inverse square of the pathlength, while in practice we observe an approximately inverse linear falloff. This is consistent with a component of noise proportional to signal, presumably due to a combination of turbulence and photon noise. The depth of absorption lines increases in proportion to pathlength, so the net absorption:noise ratio (and thus measurement precision) remains roughly constant with pathlength.

An increased telescope diameter from 10" to 12" at 1550 m also yielded a 40% improvement in SNR, compared to a

205 theoretical increase of 44% based on the relative increase in surface area. Larger telescope diameters should therefore yield further improvements in SNR. This setup yielded the best trace gas repeatabilities, though some variability between setups occurs from the availability of suitable well-mixed atmospheric periods and underlying atmospheric variability.

Finally, comparing period 5 with the Heidelberg reference performance in Table 3 at almost identical pathlength, the new system has four times better SNR and repeatability six times (0.28 ppm) and ten times (2.1 ppb) better for CO_2 and CH_4,

210 respectively, than the original system described by Griffith et al. (2018).

4.2 Comparison to in situ measurements

The time series of OP-NIR and CRDS measurements and their differences are shown in Figure 6. In the majority of the time series the two instruments capture the same broad events and the OP-NIR compares reasonably well with the Picarro

measurements over the concurrent measurement period. The OP-NIR measurements typically exhibit less variability than the in situ measurements, especially at night and/or during low windspeed conditions. This is expected, because the OP-NIR measures the spatial average of gas mole fractions, and thus variability, along the path averaged over the time of each OP-NIR measurement - 3 minutes in this case. In contrast, in situ techniques are sensitive to spatio-temporal variability at their location on the time scale of several seconds, such as localised gas fluxes and/or atmospheric mixing or lack thereof.

The comparison between the OP-NIR and Picarro for CO_2 is shown in Figure 7. The measurements are divided into three categories: sunny (solar radiation above 100 W m^{-2}), well-mixed (wind speed greater than 2 m s^{-1}) and all other data. Picarro CO_2 measurements are consistently higher at night and lower during the day in sunny periods compared to the OP-NIR measurements. Usually over grassland such as at the field site, there is a net flux of CO_2 from the atmosphere to the biosphere during the day, due to photosynthetic uptake being larger than respiration. The reverse is true at night. These fluxes establish a vertical CO_2 gradient near the Earth's surface, with higher CO_2 near the surface during the night, and lower CO_2 near the surface during the day. The CRDS inlet is closer to the surface (2.5 m) than the mean height of the OP-NIR path (23 m, see Figure 8), which may explain why the Picarro CO_2 measurements are higher at night and lower during the day than the OP-NIR.

For CH_4 (Figure 9) variations in both directions occur with the OP-NIR measurements often higher than the CRDS. This is due to the presence of two local sources in the fields over which the open-path beam passes - a coal-seam gas (CSG) well located almost directly under the path at 500m from the retroreflector, and grazing stock (sheep and cattle) most often located around the eastern end of the path. The CRDS is located to the western side of the field and since it is a point rather than path-integrated measurement, it therefore samples less influence from these sources.

A polar bivariate plot for CH_4 from open-path measurements is shown for the data from the entire campaign in Figure 10. Highest CH_4 values are seen under conditions with low wind speeds, indicating a source under or very close to the measurement path and/or a build-up of CH_4 under stable atmospheric conditions. Other high amounts are also seen from a sector to the south east, with some enhancements to the north. The nearest CSG well is located approximately 5m to the south of the open-path, 500m from the retroreflector end of the 1500m path. When they were in nearby fields, the majority of sheep were located to the east/south-east of the instrument shed (south of the retroreflector), while cattle were periodically located to the south-east of the instrument, and regularly to the north. As the experiment was conducted remotely, we do not have exact records of stock movements. The locations of the potential sources are illustrated in Figure 8.

For CH_4, an additional criterion is therefore added to the definition of well-mixed conditions to account for the CSG well, sheep and cattle that are present near to the OP-NIR measurement path. We therefore also include only data from the westerly sector in our definition of well-mixed conditions; i.e. wind directions between 180 and 360 degrees.

Comparison between the in situ CRDS measurements and the path-averaged FTIR measurements under well-mixed conditions is used to assess the bias of the OP-NIR system. Under these conditions, the relationship between the OP-NIR and CRDS falls tightly on a line. For CO_2, this corresponds to a slope of 1.0141 ± 0.0002 (r=0.89; i.e. the OP-NIR is biased high by 1.41% ($\approx$6 ppm at 400 ppm) relative to the in situ measurement scale. Figure 9 shows the comparison between in situ and open-path CH_4. With wind speeds above 2 m s^{-1} from the west, the relationship between the open-path and in situ measurements lies

around a slope of 1.0161 ± 0.0004 (r=0.89). There is much more scatter in the relationship for CH_4 than CO_2, indicative of the variety and spatial inhomogeneity of local sources and sinks. For both CO_2 and CH_4, these biases are approximately a factor of 2 smaller using HITRAN 2016 line parameters compared to HITRAN 2008 used in Griffith et al. (2018).

The comparison between the OP-NIR and in situ measurements is summarised in Table 4.

4.3 Future Directions

At EMAI, we were limited to testing up to 1.55 km due to the availability of appropriate lines-of-sight, but the pathlength-independent behaviour of the OP-NIR measurement repeatability out to 1500 m suggests that longer pathlengths are possible. Given the cost-effective BK7 glass retroreflectors, the surface area of the retroreflector array could be further increased to facilitate this. A larger telescope could also increase signal, enabling longer pathlengths to be used. The inexpensive nature of the retroreflectors, and the use of the AIM unit with programmable pointing, means that a multiple path configuration would also be possible. This could produce a doubling of effective pathlength or enable setups where upwind/downwind measurement pairs can be taken over wider areas than previously possible with the OP-MIR system (Cartwright et al., 2019; Feitz et al., 2018).

The ability to co-retrieve CO and N_2O would enable the system to be used in a broader range of applications, in both urban and rural settings. At moderate increased expense, alternative glass retroreflectors could be used to improve signal at these wavelengths, which should lead to improved precision. These co-retrieved gases could help to identify and quantify atmospheric signals especially from combustion (CO) or soil/wastewater processes (N_2O).

Open-path measurements are more likely to capture point source emissions than single point measurements provided that the repeatability is good enough to resolve this over the integrated path. The OP-NIR spatial scale is more comparable to the scale of many atmospheric models, which facilitates model intercomparison studies. Other potential applications include measurements from industrial scale composting, landfills, and wastewater treatment, agricultural monitoring of soil (fertiliser) or animal emissions, and gas pipeline monitoring and leak detection when combined with appropriate modeling.

5 Conclusions

In this paper, we present refinements to an open-path Fourier Transform Infrared system measuring in the near infrared spectral region. Over paths up to 1.55 km one-way, the system can achieve repeatability of better than 0.1% (at 0.28 ppm) for CO_2 and close to 0.1% (at 2.1 ppb) for CH_4 for 3 minute averaging times under well-mixed atmospheric conditions. The measurement precision is essentially independent of pathlength. Comparison to co-located in situ measurements, also under well-mixed conditions, indicates offsets of approximately 1.5% from measurements traceable to WMO scales. The open-path measurements therefore have a calibration offset of 1.41% for CO_2 and 1.61% for CH_4. The open-path measurements also prove capable of detecting signals from photosynthesis, respiration, and ruminant stock on local scales.

References

Alden, C. B., Coburn, S. C., Wright, R. J., Baumann, E., Cossel, K., Perez, E., Hoenig, E., Prasad, K., Coddington, I., and Rieker, G. B.: Single-Blind Quantification of Natural Gas Leaks from 1 km Distance Using Frequency Combs, Environmental Science & Technology, 53, 2908–2917, https://doi.org/10.1021/acs.est.8b06259, https://doi.org/10.1021/acs.est.8b06259, pMID: 30695644, 2019.

Allan, D. W.: Statistics of Atomic Frequency Standards, Proceedings of the IEEE, https://doi.org/10.1109/PROC.1966.4634, 1966.

Bai, M., Suter, H., Lam, S. K., Davies, R., Flesch, T. K., and Chen, D.: Gaseous emissions from an intensive vegetable farm measured with slant-path FTIR technique, Agricultural and Forest Meteorology, 258, 50–55, https://doi.org/10.1016/j.agrformet.2018.03.001, 2018.

Cartwright, L., Zammit-Mangion, A., Bhatia, S., Schroder, I., Phillips, F., Coates, T., Negandhi, K., Naylor, T., Kennedy, M., Zegelin, S., Wokker, N., Deutscher, N. M., and Feitz, A.: Bayesian atmospheric tomography for detection and quantification of methane emissions: application to data from the 2015 Ginninderra release experiment, Atmospheric Measurement Techniques, 12, 4659–4676, https://doi.org/10.5194/amt-12-4659-2019, https://www.atmos-meas-tech.net/12/4659/2019/, 2019.

Crosson, E. R.: A cavity ring-down analyzer for measuring atmospheric levels of methane, carbon dioxide, and water vapor, Applied Physics B: Lasers and Optics, 92, 403–408, https://doi.org/10.1007/s00340-008-3135-y, https://link.springer.com/content/pdf/10.1007{%}2Fs00340-008-3135-y.pdf, 2008.

Desservettaz, M., Phillips, F., Naylor, T., Price, O., Samson, S., Kirkwood, J., and Paton-Walsh, C.: Air Quality Impacts of Smoke from Hazard Reduction Burns and Domestic Wood Heating in Western Sydney, Atmosphere, 10, 557, https://doi.org/10.3390/atmos10090557, https://www.mdpi.com/2073-4433/10/9/557, 2019.

Dobler, J. T., Harrison, F. W., Browell, E. V., Lin, B., McGregor, D., Kooi, S., Choi, Y., and Ismail, S.: Atmospheric CO2 column measurements with an airborne intensity-modulated continuous wave 1.57 μm fiber laser lidar, Appl. Opt., 52, 2874–2892, https://doi.org/10.1364/AO.52.002874, http://ao.osa.org/abstract.cfm?URI=ao-52-12-2874, 2013.

Feitz, A., Schroder, I., Phillips, F., Coates, T., Negandhi, K., Day, S., Luhar, A., Bhatia, S., Edwards, G., Hrabar, S., Hernandez, E., Wood, B., Naylor, T., Kennedy, M., Hamilton, M., Hatch, M., Malos, J., Kochanek, M., Reid, P., Wilson, J., Deutscher, N., Zegelin, S., Vincent, R., White, S., Ong, C., George, S., Maas, P., Towner, S., Wokker, N., and Griffith, D.: The Ginninderra CH4 and CO2 release experiment: An evaluation of gas detection and quantification techniques, International Journal of Greenhouse Gas Control, 70, 202 – 224, https://doi.org/https://doi.org/10.1016/j.ijggc.2017.11.018, http://www.sciencedirect.com/science/article/pii/S1750583617306862, 2018.

Flesch, T. K., Baron, V. S., Wilson, J. D., Griffith, D. W., Basarab, J. A., and Carlson, P. J.: Agricultural gas emissions during the spring thaw: Applying a new measurement technique, Agricultural and Forest Meteorology, 221, 111–121, https://doi.org/10.1016/j.agrformet.2016.02.010, 2016.

Gordon, I. E., Rothman, L. S., Hill, C., Kochanov, R. V., Tan, Y., Bernath, P. F., Birk, M., Boudon, V., Campargue, A., Chance, K. V., Drouin, B. J., Flaud, J. M., Gamache, R. R., Hodges, J. T., Jacquemart, D., Perevalov, V. I., Perrin, A., Shine, K. P., Smith, M. A., Tennyson, J., Toon, G. C., Tran, H., Tyuterev, V. G., Barbe, A., Császár, A. G., Devi, V. M., Furtenbacher, T., Harrison, J. J., Hartmann, J. M., Jolly, A., Johnson, T. J., Karman, T., Kleiner, I., Kyuberis, A. A., Loos, J., Lyulin, O. M., Massie, S. T., Mikhailenko, S. N., Moazzen-Ahmadi, N., Müller, H. S., Naumenko, O. V., Nikitin, A. V., Polyansky, O. L., Rey, M., Rotger, M., Sharpe, S. W., Sung, K., Starikova, E., Tashkun, S. A., Auwera, J. V., Wagner, G., Wilzewski, J., Wcisło, P., Yu, S., and Zak, E. J.: The HITRAN2016 molecular spectroscopic database, Journal of Quantitative Spectroscopy and Radiative Transfer, 203, 3–69, https://doi.org/10.1016/j.jqsrt.2017.06.038, 2017.

Griffith, D. W. T.: Synthetic Calibration and Quantitative Analysis of Gas-Phase FT-IR Spectra, Appl. Spectrosc., 50, 59–70, http://as.osa.org/abstract.cfm?URI=as-50-1-59, 1996.

Griffith, D. W. T., Pöhler, D., Schmitt, S., Hammer, S., Vardag, S. N., and Platt, U.: Long open-path measurements of greenhouse gases in air using near-infrared Fourier transform spectroscopy, Atmospheric Measurement Techniques, 11, 1549–1563, https://doi.org/10.5194/amt-11-1549-2018, https://www.atmos-meas-tech.net/11/1549/2018/, 2018.

Humphries, R., Jenkins, C., Leuning, R., Zegelin, S., Griffith, D., Caldow, C., Berko, H., and Feitz, A.: Atmospheric Tomography: A Bayesian Inversion Technique for Determining the Rate and Location of Fugitive Emissions, Environ. Sci. Technol., 46, 1739–1746, https://doi.org/10.1021/es202807s, 2012.

Jones, F. M., Phillips, F. A., Naylor, T., and Mercer, N. B.: Methane emissions from grazing Angus beef cows selected for divergent residual feed intake, Animal Feed Science and Technology, 166-167, 302–307, https://doi.org/10.1016/j.anifeedsci.2011.04.020, 2011.

Laubach, J., Bai, M., Pinares-Patiño, C. S., Phillips, F. A., Naylor, T. A., Molano, G., Cárdenas Rocha, E. A., and Griffith, D. W.: Accuracy of micrometeorological techniques for detecting a change in methane emissions from a herd of cattle, Agricultural and Forest Meteorology, 176, 50–63, https://doi.org/10.1016/j.agrformet.2013.03.006, 2013.

Lian, J., Bréon, F.-M., Broquet, G., Zaccheo, T. S., Dobler, J., Ramonet, M., Staufer, J., Santaren, D., Xueref-Remy, I., and Ciais, P.: Analysis of temporal and spatial variability of atmospheric CO_2 concentration within Paris from the GreenLITE™ laser imaging experiment, Atmospheric Chemistry and Physics, 19, 13 809–13 825, https://doi.org/10.5194/acp-19-13809-2019, https://www.atmos-chem-phys.net/19/13809/2019/, 2019.

Loh, Z., Leuning, R., Zegelin, S., Etheridge, D., Bai, M., Naylor, T., and Griffith, D.: Testing Lagrangian atmospheric dispersion modelling to monitor CO_2 and CH_4 leakage from geosequestration, Atmospheric Environment, 43, 2602–2611, https://doi.org/10.1016/j.atmosenv.2009.01.053, 2009.

Naylor, T. A., Wiedemann, S. G., Phillips, F. A., Warren, B., McGahan, E. J., and Murphy, C. M.: Emissions of nitrous oxide, ammonia and methane from Australian layer-hen manure storage with a mitigation strategy applied, Animal Production Science, 56, 1367, https://doi.org/10.1071/AN15584, http://www.publish.csiro.au/?paper=AN15584, 2016.

Nikodem, M., Plant, G., Sonnenfroh, D., and Wysocki, G.: Open-path sensor for atmospheric methane based on chirped laser dispersion spectroscopy, Applied Physics B: Lasers and Optics, 119, 3–9, https://doi.org/10.1007/s00340-014-5938-3, https://link.springer.com/article/10.1007/s00340-014-5938-3, 2015.

Phillips, F. A., Wiedemann, S. G., Naylor, T. A., McGahan, E. J., Warren, B. R., Murphy, C. M., Parkes, S., and Wilson, J.: Methane, nitrous oxide and ammonia emissions from pigs housed on litter and from stockpiling of spent litter, Animal Production Science, 56, 1390–1403, https://doi.org/10.1071/AN15650, 2016.

Phillips, F. A., Naylor, T., Forehead, H., Griffith, D. W., Kirkwood, J., and Paton-Walsh, C.: Vehicle ammonia emissions measured in an urban environment in Sydney, Australia, using open path fourier transform infra-red spectroscopy, Atmosphere, 10, https://doi.org/10.3390/ATMOS10040208, 2019.

Plant, G., Nikodem, M., Mulhall, P., Varner, R., Sonnenfroh, D., and Wysocki, G.: Field Test of a Remote Multi-Path CLaDS Methane Sensor, Sensors, 15, 21 315–21 326, https://doi.org/10.3390/s150921315, http://www.mdpi.com/1424-8220/15/9/21315, 2015.

Queisser, M., Granieri, D., and Burton, M.: A new frontier in CO2 flux measurements using a highly portable DIAL laser system, SCIENTIFIC REPORTS, 6, https://doi.org/10.1038/srep33834, 2016.

Rieker, G. B., Giorgetta, F. R., Swann, W. C., Kofler, J., Zolot, A. M., Sinclair, L. C., Baumann, E., Cromer, C., Petron, G., Sweeney, C., Tans, P. P., Coddington, I., and Newbury, N. R.: Frequency-comb-based remote sensing of greenhouse gases over kilometer air paths, Optica, 1, 290–298, https://doi.org/10.1364/OPTICA.1.000290, http://www.osapublishing.org/optica/abstract.cfm?URI=optica-1-5-290, 2014.

365   Rothman, L., Gordon, I., Barbe, A., Benner, D., Bernath, P., Birk, M., Boudon, V., Brown, L., Campargue, A., Champion, J.-P., Chance, K., Coudert, L., Dana, V., Devi, V., Fally, S., Flaud, J.-M., Gamache, R., Goldman, A., Jacquemart, D., Kleiner, I., Lacome, N., Lafferty, W., Mandin, J.-Y., Massie, S., Mikhailenko, S., Miller, C., Moazzen-Ahmadi, N., Naumenko, O., Nikitin, A., Orphal, J., Perevalov, V., Perrin, A., Predoi-Cross, A., Rinsland, C., Rotger, M., Šimečková, M., Smith, M., Sung, K., Tashkun, S., Tennyson, J., Toth, R., Vandaele, A., and Auwera, J. V.: The HITRAN 2008 molecular spectroscopic database, Journal of Quantitative Spectroscopy and Radia-

370   tive Transfer, 110, 533 – 572, https://doi.org/https://doi.org/10.1016/j.jqsrt.2009.02.013, http://www.sciencedirect.com/science/article/pii/S0022407309000727, hITRAN, 2009.

Saito, H., Manago, N., Kuriyama, K., and Kuze, H.: Near-infrared open-path measurement of CO2 concentration in the urban atmosphere, OPTICS LETTERS, 40, 2568–2571, https://doi.org/10.1364/OL.40.002568, 2015.

Wagner, G. A. and Plusquellic, D. F.: Ground-based, integrated path differential absorption LIDAR measurement of CO_2,

375   CH_4, and H_2O near 16 μm, Applied Optics, 55, 6292, https://doi.org/10.1364/ao.55.006292, https://www.osapublishing.org/viewmedia.cfm?uri=ao-55-23-6292{&}seq=0{&}html=truehttps://www.osapublishing.org/abstract.cfm?uri=ao-55-23-6292https://www.osapublishing.org/ao/abstract.cfm?uri=ao-55-23-6292, 2016.

Waxman, E. M., Cossel, K. C., Truong, G.-W., Giorgetta, F. R., Swann, W. C., Coburn, S., Wright, R. J., Rieker, G. B., Coddington, I., and Newbury, N. R.: Intercomparison of open-path trace gas measurements with two dual-frequency-comb spectrometers, Atmospheric

380   Measurement Techniques, 10, 3295–3311, https://doi.org/10.5194/amt-10-3295-2017, https://www.atmos-meas-tech.net/10/3295/2017/, 2017.

Werle, P., Mücke, R., and Slemr, F.: The limits of signal averaging in atmospheric trace-gas monitoring by tunable diode-laser absorption spectroscopy (TDLAS), Applied Physics B Photophysics and Laser Chemistry, https://doi.org/10.1007/BF00425997, 1993.

Wunch, D., Toon, G. C., Blavier, J.-F. L., Washenfelder, R. A., Notholt, J., Connor, B. J., Griffith, D. W., Sherlock, V., and Wennberg,

385   P. O.: The Total Carbon Column Observing Network, Philosophical Transactions of the Royal Society A: Mathematical, Physical and Engineering Sciences, 369, 2087, 2011.
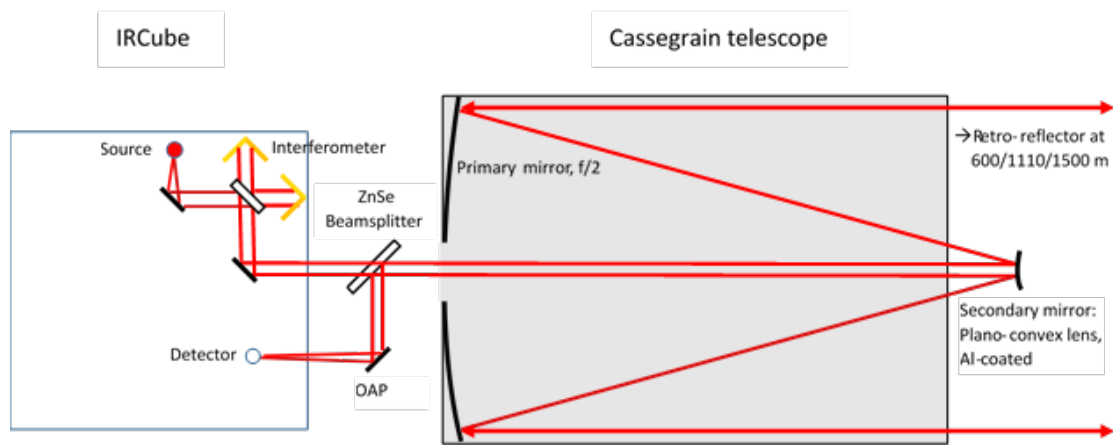
Figure 1. Schematic diagram of the setup of the OP-NIR spectrometer, its coupling to the Cassegrain telescope, and the lightpath through these and subsequent to/from the retroreflector.
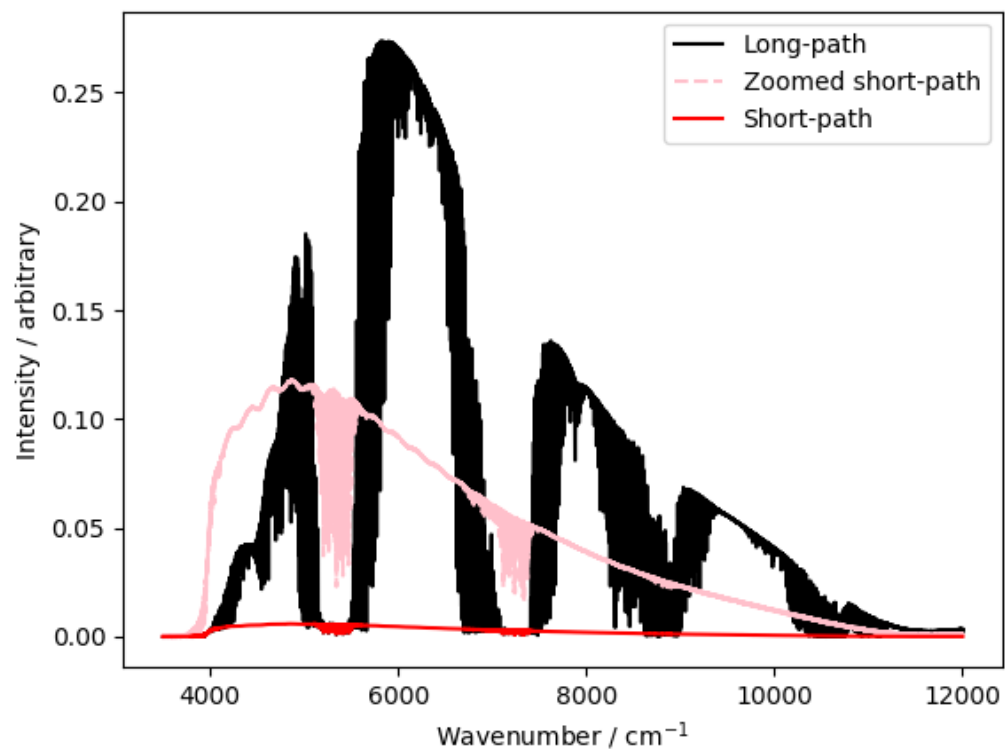
Figure 2. Example long-path spectrum (23:48 Dec 5, 2018, black) and original (red) and 20x zoom (pink) short-path spectrum (21:48 Dec 2, 2018).
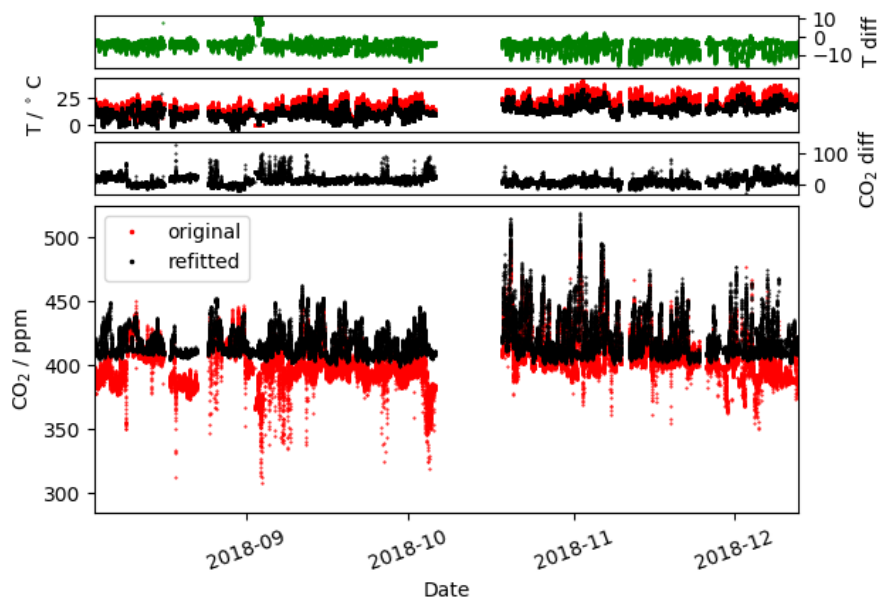
Figure 3. Timeseries illustrating the impact of re-processing the original spectra to account for contributions from short-path (spurious) reflections and inaccuracies in measured temperature. The figure shows in order from bottom to top: the original (red) and refitted (black) CO_2 (bottom), the difference between the refitted and original CO_2 (2nd from bottom), the measured (red) and fitted (black) temperature (2nd from top), and the difference between the fitted and measured temperature (top).
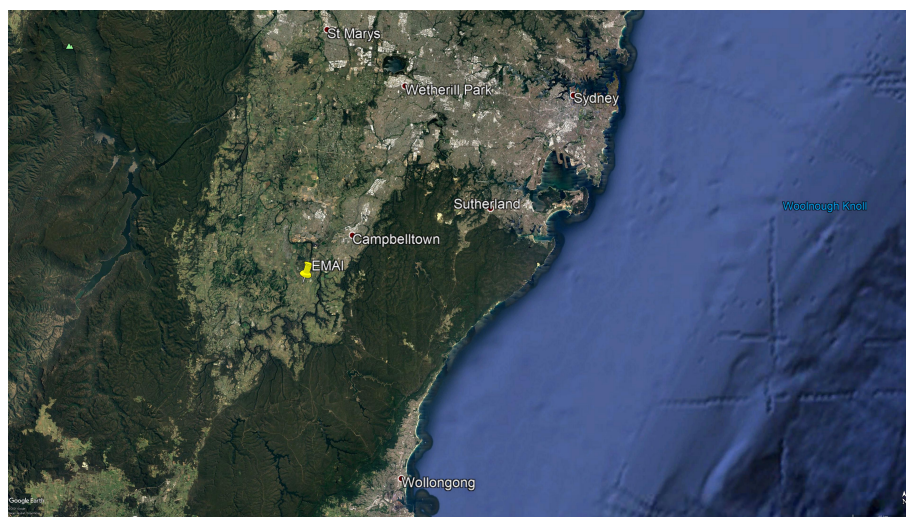
Figure 4. Map showing the location of EMAI relative to Sydney and Wollongong. The measurement path and corresponding elevation profile are shown in Figure 8. Map data © Google Earth.
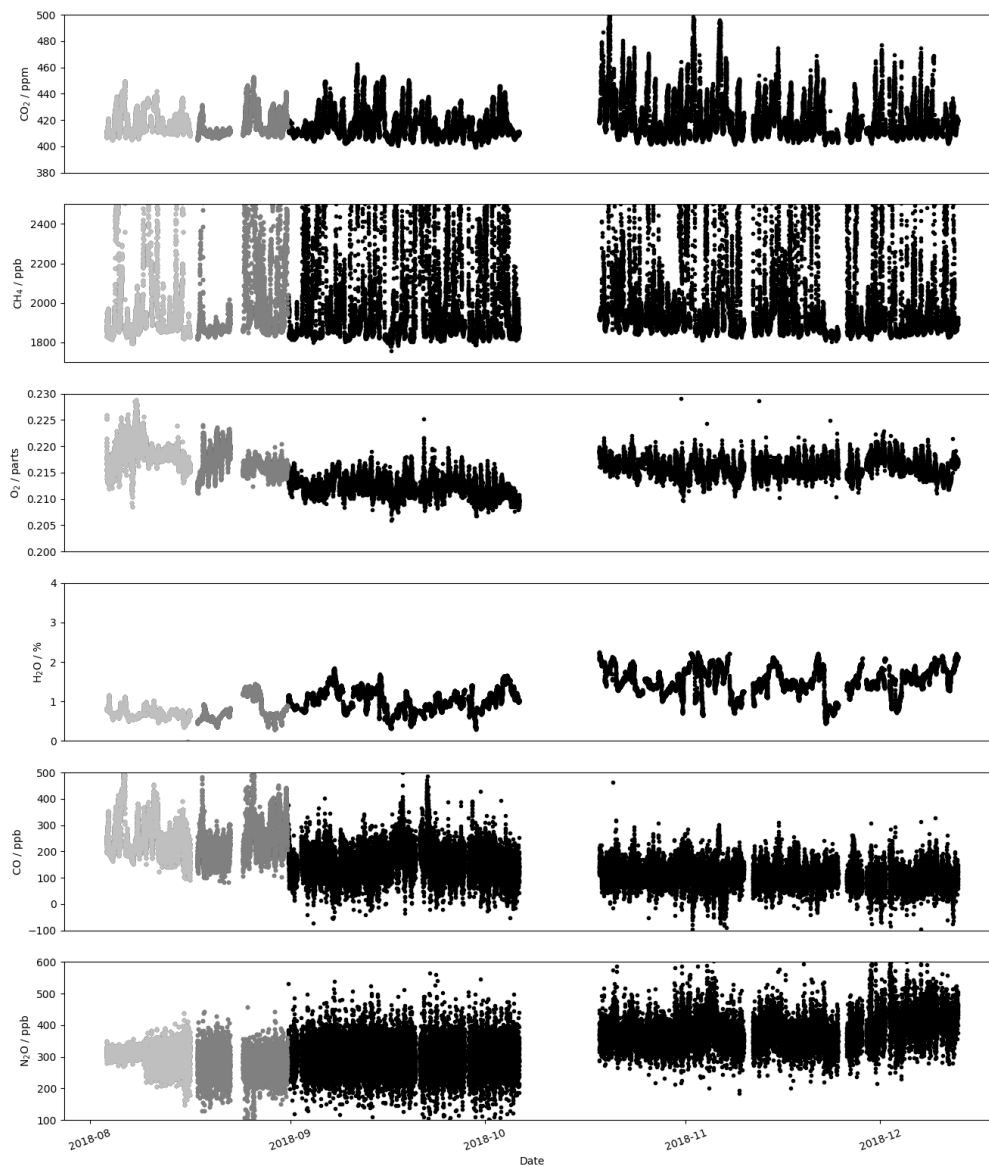
Figure 5. Time series of the retrieved path-averaged mole fractions for the 600m, 1110m and 1500m pathlengths. Data collected at a one-way pathlength of 600m are shown in light grey, at 1110m in darker grey, and the 1500m pathlength in black. The CH_4 y-axis has been zoomed to 1700 to 2500 nmol mol^{-1}.
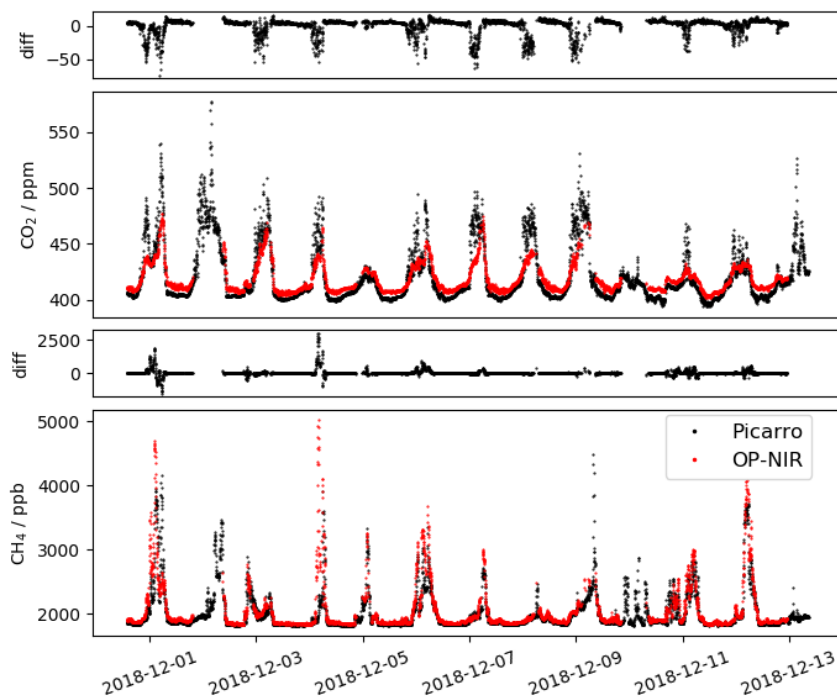
Figure 6. Time series of measured CO_2 (top) and CH_4 (bottom) from the OP-NIR (red) and in situ CRDS (black) measurements while the CRDS was co-located with the OP-NIR, from December 1-13, 2018. For each gas, the upper panel shows the difference between the OP-NIR and CRDS measurements.
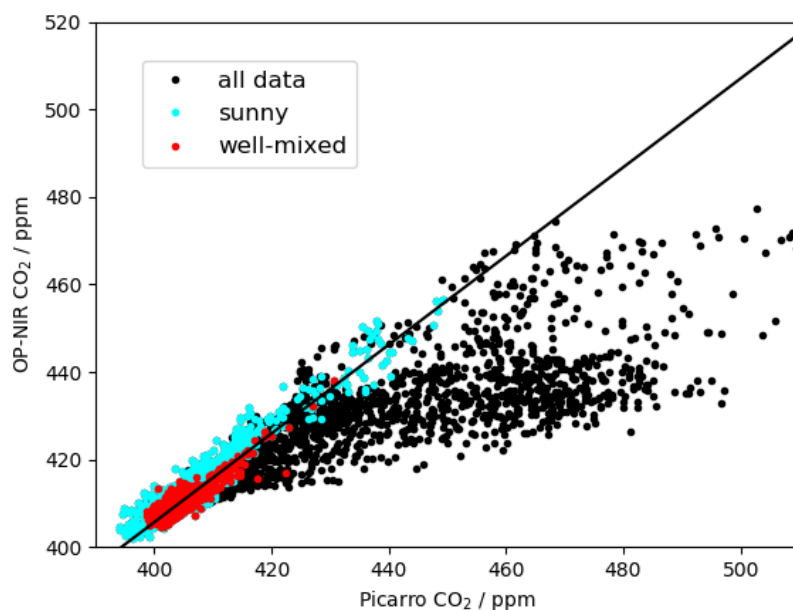
Figure 7. Comparison of path-averaged CO_2 measured by the open-path NIR and in situ CO_2 measured by the CRDS. All data points are shown in black, with those from well-mixed conditions (wind speeds greater than 2 m s^{-1}) in red, and those during sunlight hours (solar radiation greater than 100 W m^{-2}) in cyan. The best fit line (OP-NIR = 1.0141 $\pm$ 0.0002 * Picarro) for the fit of OP-NIR vs in situ measurements under well-mixed conditions is shown.
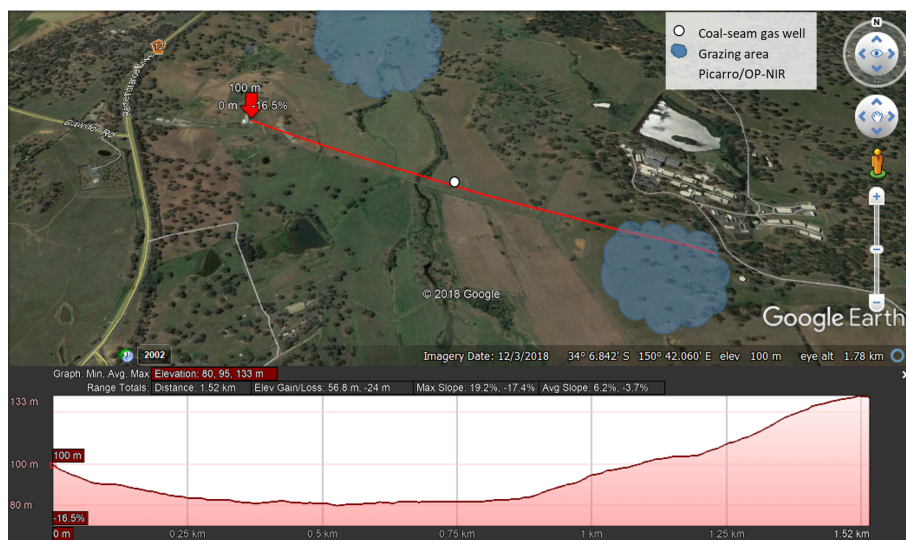
Figure 8. Map of the 1.55 km path at EMAI and corresponding elevation profile. The OP-NIR and stationary Picarro were located at the left end of the path and the retroreflector array at the right end. The mean elevation across the 1.55 km observation path is 118 metres above sea level an average of 23 metres above surface elevation. Map © Google Earth.
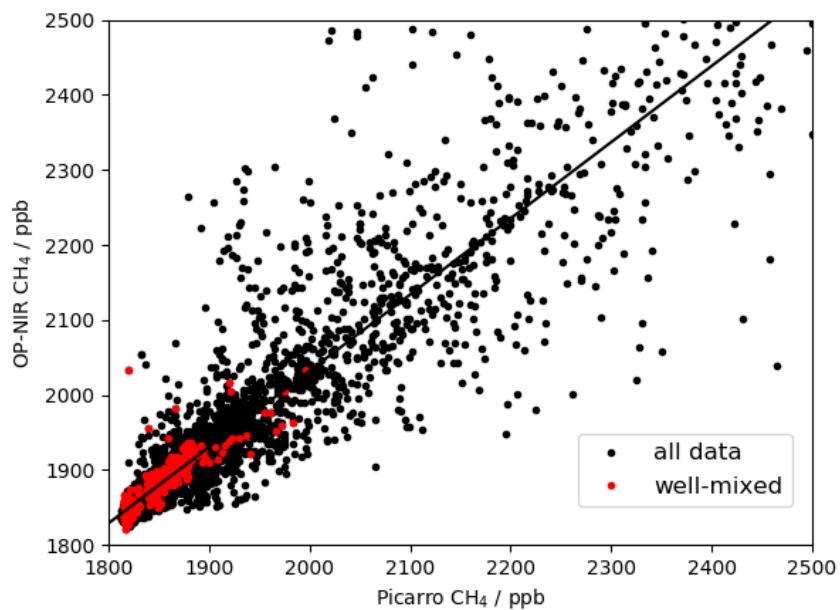
Figure 9. Comparison of path-averaged CH$_4$ measured by the open-path NIR and in situ CH$_4$ measured by the CRDS. All data points are shown in black, with those from well-mixed conditions (wind speeds greater than 2 m s^{-1} and from the westerly sector) in red. The best fit line of OP-NIR = 1.0161 $\pm$ 0.0004 * Picarro for the fit of OP-NIR vs in situ measurements under well-mixed conditions is shown.
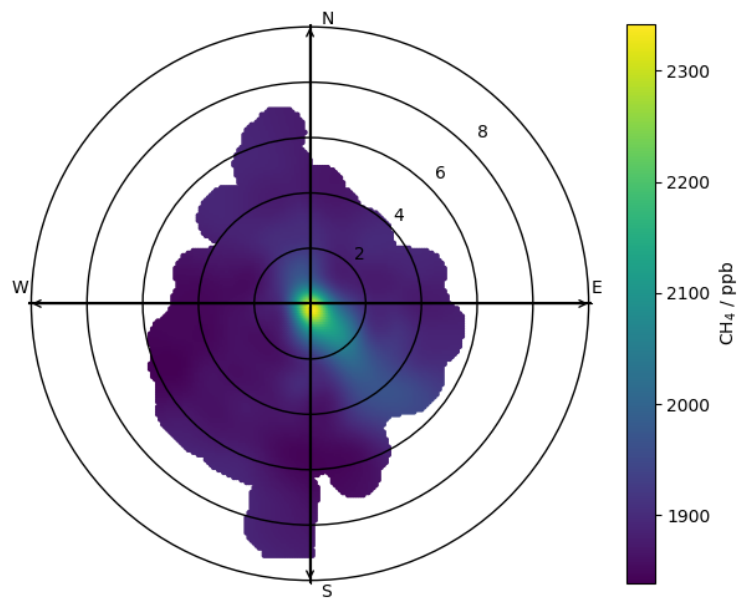
Figure 10. Polar bivariate plot showing the relationship between CH_4, wind speed and wind direction over the full campaign.

Table 1. Summary of the spectral windows used for retrieval of path-averaged concentrations in the open-path NIR spectra, see Griffith et al. (2018) for plots.

Gas fitted	Interfering species	Spectral region / cm^{-1}
O_2	H_2O	7790 - 7960
CO_2	H_2O	4800 - 5050
CH_4	H_2O	5885 - 6150
H_2O, HDO	CO_2	4910 - 5080
CO	H_2O	4260 - 4310
N_2O	CH_4, H_2O	4300 - 4460

Table 2. Summary of open-path NIR instrument setup at EMAI. Previous work by Griffith et al. (2018) in Heidelberg is used as a reference.

Measurement Period	Start Date	End Date	Pathlength (one-way)	Retroreflector	Telescope diameter
1	20180804	20180809	600m	Hollow gold-coated	10"
2	20180809	20180816	600m	Solid uncoated BK7 glass	10"
3	20180816	20180831	1110m	Solid uncoated BK7 glass	10"
4	20180831	20181008	1500m	Solid uncoated BK7 glass	10"
5	20181018	20181212	1500m	Solid uncoated BK7 glass	12"
ref	201407	201411	1500m	solid UV quartz	12"

Table 3. Summary of the measurement performance during the field deployment at each pathlength and over changes in instrument setup. The numbered measurement periods and setups correspond to those in Table 2.

Measurement period	Instrument setup (path, reflector, telescope)	Signal-to-noise ratio (SNR)	Repeatability (1σ)			
			CO_2 / ppm	CH_4 / ppb	CO / ppb	N_2O / ppb
1	600m, gold, 10"	2050	0.74	8.5	7.0	8.4
2	600m, glass, 10"	6400	0.60	14.8	24.2	30.9
3	1110m, glass, 10"	3750	0.38	3.8	27.1	35.8
4	1500m, glass, 10"	2300	0.46	3.9	28.5	35.6
5	1500m, glass, 12"	3200	0.28	2.1	17.1	21.8
ref[#]	1500m, quartz, 12"	750	1.7	21	-	-

[#]Deployment at Heidelberg (Griffith et al., 2018).

Table 4. Calculated biases of OP-NIR measurements relative to either in situ measurements or known mole fractions.

Species	Ratio (mean $\pm$ s.d.)	r
CO_2	1.0141 ± 0.0002	0.89
CH_4	1.0161 ± 0.0004	0.89
O_2	1.0266 ± 0.0001	N/A